# Estimating Enhancement Ratios of Nitrogen Dioxide, Carbon Monoxide and Carbon Dioxide using Satellite Observations

Cameron G. MacDonald[1,2,3], Joshua L. Laughner[4], Jacob K. Hedelius[5], Ray Nassar[6], Jon-Paul Mastrogiacomo[1], and Debra Wunch[1]

[1]University of Toronto, Department of Physics, Toronto, Ontario, Canada
[2]University of Waterloo, Department of Physics and Astronomy, Waterloo, Ontario, Canada
[3]Princeton University, Program in Atmospheric and Oceanic Sciences, Princeton, New Jersey, USA
[4]Jet Propulsion Laboratory, California Institute of Technology, Pasadena, California, USA
[5]Space Dynamics Laboratory, Utah State University, North Logan, Utah, USA
[6]Climate Research Division, Environment and Climate Change Canada, Toronto, Ontario, Canada

**Correspondence:** Debra Wunch (dwunch@atmosp.physics.utoronto.ca)

**Abstract.**

Using co-located space-based measurements of carbon dioxide ($CO_2$) from the Orbiting Carbon Observatory 2 and 3 (OCO-2/3) and carbon monoxide (CO) and nitrogen dioxide ($NO_2$) from the Tropospheric Monitoring Instrument (TROPOMI), we calculate total column enhancements for observations influenced by anthropogenic emissions from urban regions relative to

5   clean background values. We apply this method to observations taken over or downwind of 27 large (> 1 million population) urban areas from around the world. Enhancement ratios between species are calculated and compared to emission ratios derived from four globally gridded anthropogenic emission inventories. We find that these global inventories underestimate CO emissions in many North American and European cities relative to our observed enhancement ratios, while smaller differences were found for $NO_2$ emissions. We further demonstrate that the calculation and intercomparison of enhancement ratios of multiple

10   tracers can help to identify the underlying biases leading to disagreement between observations and inventories. Additionally, we use high-resolution $CO_2$ inventories for two cities (Los Angeles and Indianapolis) to estimate emissions of CO and $NO_2$ using our calculated enhancement ratios, and find good agreement with both a previous modelling study for the Los Angeles megacity and California Air Resource Board (CARB) inventory estimates.

## 1   Introduction

15   Improving air quality and reducing greenhouse gas emissions are focuses of environmental policy from the global to municipal levels (Gurney et al., 2018a). Emissions inventories provide information about the distribution and sources of air pollution and greenhouse gas emissions as well as their trends over time. These inventories are constructed using bottom-up approaches: Information on socio-economic activity is used alongside expected emissions factors for these activities to model emissions (Gurney et al., 2012; Janssens-Maenhout et al., 2019). Atmospheric measurements have been shown to be useful as part of

20   top-down approaches in validating and refining these emissions inventories (McKain et al., 2012; Duren and Miller, 2012).

The expansion of the constellation of Earth-observing satellites taking measurements of greenhouse gases and air pollutants has led to observations over urban regions with unprecedented spatiotemporal coverage. Kort et al. (2012) used observations from the Greenhouse Gases Observing SATellite (GOSAT), launched January 2009, to measure enhancements of atmospheric carbon dioxide ($CO_2$) over megacities. Since the launch of the Orbiting Carbon Observatory-2 (OCO-2) in July 2014 (Crisp
25   et al., 2004), further studies have characterized emissions from urban regions (e.g., Wu et al., 2018; Reuter et al., 2019). The Orbiting Carbon Observatory-3 (OCO-3) aboard the International Space Station (ISS) since May 2019 (Eldering et al., 2019) has provided additional observations of $CO_2$ in urban areas (Kiel et al., 2021). Satellite remote sensing of additional air pollutants has been greatly expanded with the launch of the TROPOspheric Monitoring Instrument (TROPOMI) aboard the Sentinel-5 Precursor (S5P) satellite on 13 October 2017 (Veefkind et al., 2012). Early investigations into the TROPOMI carbon
30   monoxide (CO) and nitrogen dioxide ($NO_2$) products have shown the ability of TROPOMI to map concentrations of these air pollutants at the city-scale (e.g., Borsdorff et al., 2018; Zhao et al., 2020).

Enhancement ratios have been shown to be useful in evaluating the validity of emissions inventories and estimating emissions from a variety of anthropogenic sources of greenhouse gases and air pollutants. Wunch et al. (2009) used a ground-based remote sensing instrument to measure the diurnal variation of greenhouse gases within California's South Coast Air Basin
35   (SoCAB) and calculate enhancement ratios between $CO_2$, CO, $CH_4$ and $N_2O$. Hedelius et al. (2018) used a combination of ground-based and satellite-based remote sensing instruments and a Lagrangian particle dispersion model to derive improved enhancement and emissions ratios between $CO_2$, CO and $CH_4$ for the SoCAB, while also demonstrating good agreement between ratios computed using different methods. Enhancement ratio methods involving both greenhouse gases (primarily $CO_2$) and air pollutants have also been used to investigate the combustion characteristics of anthropogenic activities; Silva
40   and Arellano (2017) used satellite measurements of $CO_2$, $NO_2$ and CO to show a correlation between the dominant forms of combustion and both $NO_2$:CO and CO:$CO_2$ enhancement ratios in 14 regions from around the world. More recently, Lama et al. (2020) used measurements from TROPOMI to investigate burning efficiencies in six megacities by computing $NO_2$:CO enhancement ratios and comparing to emissions ratios from global inventories. Plant et al. (2022) used TROPOMI methane and CO enhancements to assess methane emissions from several US cities.

45   In this paper, we describe a method to compute enhancement ratios between $CO_2$, CO and $NO_2$ over 27 large urban areas by combining measurements from three different space-based instruments. We use measurements of atmospheric $CO_2$ from OCO-2 and OCO-3 and measurements of CO and $NO_2$ from TROPOMI to measure anomalies over urban areas relative to a regional background. Results across multiple overpasses of these urban regions are used to derive enhancement ratios, which are then compared to ratios calculated from four global emissions inventories: The Emissions Database for Global Atmospheric
50   Research (EDGAR), The Open Source Data Inventory for Anthropogenic $CO_2$ (ODIAC), the Fossil Fuel Data Assimilation System (FFDAS) and the Mapping Atmospheric Chemistry and Climate and CityZen (MACCity) inventory.

In section 2, we will describe the datasets and global emission inventories used in our analyses. In section 3, we will describe our approach to derive enhancement ratios between gases from satellite measurements. Section 4 will present the results of this analysis and section 5 will discuss the implications of these findings. Finally, section 6 will summarize our conclusions and
55   suggest future work.

## 2 Data

### 2.1 OCO-2

We use measurements of the column averaged dry air mole fraction of carbon dioxide ($X_{CO_2}$) from OCO-2 (Crisp et al., 2004). OCO-2 was launched on 2 July 2014 into a sun-synchronous orbit with an equator crossing time of about 13:30 (ascending node) as part of the afternoon constellation (or A-train) of satellites. OCO-2 has been collecting science measurements of ($X_{CO_2}$) since 6 September 2014, collecting around 1 million total column observations per day (Crisp et al., 2017). The OCO-2 instrument includes three different grating spectrometers that measure reflected solar radiation in the near-infrared (NIR) and shortwave infrared (SWIR) spectral regions. The spectral bands include the $O_2$ A-Band from 0.7576—0.7726 $\mu$m, along with the "weak" and "strong" $CO_2$ bands measured at 1.5906—1.6218 and 2.0431—2.0834 $\mu$m, respectively. Measurements are taken in a horizontal row with 8 cross-track footprints, with 3 rows of observations collected every second. Each individual footprint has dimensions of approximately 2.25 km in the along-track direction and up to 1.29 km in the cross-track direction (depending on the satellite orientation). OCO-2 observes in three different modes of operation. In nadir mode, the observations are taken at the sub-satellite point and measurements taken over water are typically filtered out. In glint mode, the satellite makes observations near the point of the Earth's surface where sunlight is specularly reflected (Crisp et al., 2017; Eldering et al., 2019). Finally, OCO-2 can operate in a target mode, where a small area of the Earth is observed for several minutes while the satellite passes overhead. This mode is often used for the validation of measurements against ground-based remote sensing stations (e.g., Wunch et al., 2017).

For this study we use bias-corrected measurements of $X_{CO_2}$ from the OCO-2 Level 2 Lite files, version 9 (Kiel et al., 2019), accessed from the Goddard Earth Sciences Data and Information Services Center (GES-DISC) (https://disc.gsfc.nasa.gov/). The bias-correction process for OCO-2 adjusts $X_{CO_2}$ based on spurious correlations with retrieved aerosols, surface albedo and the difference between the vertical gradients of the retrieved and a priori $CO_2$ profiles. Version 9 includes an additional surface pressure based bias correction to account for pointing offsets which can cause greater uncertainties in regions with considerable topographic changes. Binary quality flags are provided in the files to indicate high and low accuracy measurements; for this study we only use measurements that have been flagged as "good".

### 2.2 OCO-3

We also use measurements of $X_{CO_2}$ from OCO-3 aboard the International Space Station (ISS). OCO-3 was launched to the ISS on 4 May 2019, and began providing science measurements on 6 August 2019. The OCO-3 instrument is a nearly identical spectrometer to OCO-2, measuring spectra in the $O_2$ A Band and weak and strong $CO_2$ bands to provide an eight footprint swath of parallelogram-shaped soundings measuring approximately 1.6 km in the cross-track direction by 2.2 km in the along-track direction, with 3 rows of observations taken every second (Eldering et al., 2019). OCO-2 pointing is carried out by maneuvers to the spacecraft, which is not possible on the ISS, thus OCO-3 is equipped with a pointing mirror assembly (PMA). In addition to the three observation modes described for OCO-2, the PMA enables OCO-3 to scan in an additional "Snapshot Area Map" (SAM) mode, where a two-dimensional area is swept out by adjacent swaths of measurements. This mode measures across

regions on the order of 100 km × 100 km, with the goal of capturing detailed maps of sources of $CO_2$ such as cities, fossil fuel

90  burning power plants and volcanoes. According to the OCO-3 SAM web-page (https://ocov3.jpl.nasa.gov/sams/index.php), between 6 August 2019 and 30 June 2020 there were over 2000 SAM maneuvers executed by OCO-3, with around half of these instances corresponding to sites influenced by anthropogenic sources of $CO_2$.

Bias-corrected measurements of $X_{CO_2}$ from the early (VEarly) release of the OCO-3 Version 10 Lite Files were accessed from the NASA GES-DISC. We found that most instances of dense measurements over cities were obtained while the instru-

95  ment was operating in SAM mode (Eldering et al., 2019).

## 2.3 TROPOMI

In our analysis, we use measurements of $NO_2$ and CO retrieved from TROPOMI observations. TROPOMI was launched on board the European Space Agency (ESA) Sentinel-5 Precursor (S5P) satellite on 13 October 2017 into a sun-synchronous orbit with an equator crossing time of about 13:30 (ascending node) and has been providing science measurements since 30 April

100  2018. TROPOMI is a nadir-viewing grating spectrometer that measures Earth-reflected solar irradiance in three spectral bands: In the ultra-violet and visible light (UV-Vis) band from 0.27–0.5 $\mu$m, an NIR band from 0.675–0.775 $\mu$m and a SWIR band from 2.305–2.385 $\mu$m (Veefkind et al., 2012). Measurements in these bands enable quantification of CO and $NO_2$, as well as methane ($CH_4$), sulfur dioxide ($SO_2$), formaldehyde (HCHO), ozone ($O_3$), and additional aerosol properties. The 2600 km wide swath of TROPOMI allows for global coverage every day (van Geffen et al., 2020) (before loss of data due to clouds).

105  ### 2.3.1 TROPOMI CO

A subset of TROPOMI measurements from the SWIR band (2.315–2.338 $\mu$m) are used to infer the total column of CO, along with corresponding column averaging kernels and error estimates under clear-sky conditions (Landgraf et al., 2016). From 30 April 2018 until 6 August 2019, TROPOMI CO pixels were 7 km × 7 km, with 215 cross-track pixels. From 6 August 2019 onward, the along-track resolution of the instrument was improved to 5.5 km. The TROPOMI data that we use is version 1 of

110  the data product.

TROPOMI total column CO values exhibit a stripe bias between adjacent rows of along-track observations (Borsdorff et al., 2018). In addition to creating offsets to adjacent observations, the magnitude of the bias can change in the along-track direction. To remove this bias we use the Fourier Filter De-striping (FFD) method described by Borsdorff et al. (2019) as a non-uniformity correction. This algorithm involves taking the two-dimensional Fourier Transform (FT) of the CO measurements from a single

115  orbit, and filtering out modes with high frequency in the cross-track direction and low frequency in the along-track direction. We identified a similar bias in the surface level values of the CO column averaging kernels, so FFD was applied to these values as well.

The quality of the measurements of the total column of CO from TROPOMI are denoted by a quality assurance value ("qa_value") provided with each observation, with 0 indicating the lowest quality and 1 the highest. Following the product user

120  manual (https://sentinel.esa.int/documents/247904/2474726/Sentinel-5P-Level-2-Product-User-Manual-Carbon-Monoxide), we use measurements with a qa_value of 0.7 or greater, which indicates clear sky conditions. Furthermore, we filter out measure-

ments taken either entirely or partially over water. Finally, we convert the provided total column in mol/m$^2$ to total column dry-air mole fractions (X$_{CO}$) in ppb as described in Wunch et al. (2016) using the retrieved total column of water and the provided surface pressure for each observation.

### 2.3.2 TROPOMI NO$_2$

Observations over 0.405–0.465 $\mu$m from the UV-Vis spectrometer in TROPOMI are used to infer the tropospheric vertical column densities of NO$_2$ (van Geffen et al., 2020). TROPOMI NO$_2$ ground sampling distance is approximately 3.5 km in the cross-track, with the same along-track distance as the CO product. Similar to the TROPOMI CO product, the quality of measurements of the tropospheric column of NO$_2$ is described by a qa_value field. Following the NO$_2$ Product User Manual (https://sentinel.esa.int/documents/247904/2474726/Sentinel-5P-Level-2-Product-User-Manual-Nitrogen-Dioxide), we use only NO$_2$ measurements with a qa_value of 0.75 or greater. No stripe bias correction is needed for the NO$_2$ product, as corrections have already been applied to the values provided in the NO$_2$ Level 2 files. Again the column densities are converted to dry-air mole fractions using the retrieved column of water and reported surface pressure. Finally, tropospheric averaging kernels are derived from the provided total column averaging kernels following the method described by Eskes et al. (2019).

### 2.4 Cities

For information on the location and extent of cities from around the world, we use the European Commission Joint Research Centre's (EC-JRC) Global Human Settlement layer Urban Centres Database (GHS-UCDB) (Florczyk et al., 2019). Though "cities" in this database are often urban agglomerations composed of multiple municipalities, we refer to an urban agglomeration as a single city for convenience. Spatial extents of over 13000 cities are determined based on the presence and density of buildings and from the population density of the region from the GHS Built-up Areas (GHS-BUILT) and GHS population density (GHS-POP) databases (Corbane et al., 2018), respectively. Polygons defining the boundaries of each city are provided on a 1 km × 1 km grid. We focus our attention primarily on cities with total populations greater than 1 million persons, where we typically observe average X$_{CO_2}$ enhancements on the order of 1 ppm compared to nearby measurements that are not influenced by anthropogenic sources. We also look at lower population cities in North America and Europe which have high per capita emissions. While emissions for smaller cities are not investigated, their presence in the dataset is often useful in explaining additional enhancements or plumes observed within the data.

### 2.5 Emissions Inventories

Bottom-up emissions inventories are used as a separate way to derive emissions ratios. Emission inventories are typically on a mass basis, and need to be converted to a molar basis for comparison with satellite-derived estimates. We derive the inventory-based ratio A:B from

$$\alpha = \left(\frac{M_B}{M_A}\right)\frac{E_A^{\text{City, Inv}}}{E_B^{\text{City, Inv}}},$$ (1)

where $M_A$ and $M_B$ are the molar masses of the respective species, and $E_A^{\text{City, Inv}}$ and $E_B^{\text{City, Inv}}$ are the total emissions estimates for the given city and inventory in mass per year. Total emissions for a city are derived by integrating the fluxes over the extent of the GHS polygon for the given city. We combine four different gridded global anthropogenic inventories to derive ratios for

155    $NO_2$:CO, $NO_2$:$CO_2$ and CO:$CO_2$.

The Open Source Data Inventory for Anthropogenic $CO_2$ (ODIAC2018) is a high resolution global emissions inventory for $CO_2$ that provides anthropogenic fluxes on an approximately 1 km $\times$ 1 km grid with monthly temporal frequency from 2000–2019 (Oda and Maksyutov, 2011). Gridded fluxes are disaggregated from total country emissions using information on strong point sources and satellite observations of night lights. The monthly estimates provided by ODIAC can be further disaggregated

160    at weekly and diurnal time scales using the Temporal Improvements for Modeling Emissions by Scaling (TIMES) scaling factors (Nassar et al., 2013) which provide gridded ($0.25° \times 0.25°$) scale factors based on both the day of the week and hour of the day.

The Fossil Fuel Data Assimilation System Version 2.2 (FFDAS) is a high resolution anthropogenic $CO_2$ emissions inventory which provides yearly fluxes for the period 1997–2015 on a $0.1° \times 0.1°$ spatial grid (Asefi-Najafabady et al., 2014). Because

165    the FFDAS time period does not extend to the operational period of TROPOMI, we use the 2015 values to derive our estimates. Similar to ODIAC, night lights data are used to disaggregate national emissions data down to a finer resolution. TIMES scaling factors are also applied to the disaggregated data in the development of FFDAS. Before being intergrated over the GHS polygon extent to get city-wide estimates, the FFDAS grid is downscaled to the ODIAC resolution, with uniform distribution across the original grid cell.

170    The EC-JRC Emissions Database for Global Atmospheric Research Version 5.0 (EDGARv5.0) is a global emissions inventory which provides gridded fluxes for many greenhouse gases and air pollutants for 1970–2015 (Crippa et al., 2020; European Commission and Joint Research Centre et al., 2019). We use the inventories for $CO_2$, CO and $NO_x$ (the combination of NO and $NO_2$). Emissions of $NO_2$ are approximated by dividing the provided $NO_x$ emissions by a factor of 1.32 (Pandis and Seinfeld, 2006). EDGAR is provided on a $0.1° \times 0.1°$ grid with yearly fluxes for the time period 1970–2015. Similar to FFDAS, we

175    apply TIMES scaling factors to the $CO_2$ inventory, and downscale the grid to the ODIAC resolution before integrating over a city region.

The final inventory that is used is the Mapping Atmospheric Chemistry and Climate and CityZen (MACCity, Granier et al., 2011). MACCity provides yearly fluxes of CO and $NO_x$ on a $0.5° \times 0.5°$ global grid from 1990–2010. As with the other inventories, MACCity was downscaled to the resolution of ODIAC before city emissions were derived. Table 1 summarizes

180    emissions estimates from these inventories for all cities that are considered in this study.

## 3   Methods

### 3.1   Co-location of OCO-2 and TROPOMI Data

Because OCO-2 and S5P have sun-synchronous orbits with similar equator crossing times and repeat cycles, there is often overlap between observations from the two instruments. We locate overpasses of cities by searching for OCO-2 observations

within 75 km of a city boundary of interest. Winds at 50 metres are chosen to represent the boundary layer and are used to filter overpasses. We interpolate from the Modern-Era Retrospective analysis for Research and Applications Version 2 (MERRA-2, Molod et al., 2015) at a spatial resolution of 0.5° latitude × 0.625° longitude and 3-hourly temporal resolution to the location and time of the overpass. When the boundary layer wind direction points away from the location of the OCO-2 swath the overpass is rejected, as the pollution plume from the city is not captured. Further filtering is performed to remove overpasses where the OCO-2 data downwind of the city is extremely sparse ( >95% of OCO-2 observations near the city flagged as bad), which is often the case when there is significant cloud cover in the region. After these filtering steps, the OCO-2 data, along with the TROPOMI data from the same time period are visualized and inspected to check for issues such as the presence of secondary sources of greenhouse gases or pollutants, and to ensure there are coincident measurements between the two satellites. During this step, corrections are applied to the MERRA-2 wind direction if considerable discrepancies are observed between the given wind bearing and the behaviour of the plume emanating from the city, which is generally most visible in the TROPOMI $NO_2$ product. Similar manual corrections have been employed in past studies using observations from OCO-2 (e.g., Nassar et al., 2017; Reuter et al., 2019; Nassar et al., 2021). At best, our manual inspections found that 83% of the overpasses which passed the initial automatic filtering were viable in a city, and at worst, all of the overpasses were rejected for a city. The median retention rate is 31% of the overpasses per city.

A similar approach is used to search for co-located measurements from OCO-3 and TROPOMI. This task is more complex as the ISS is in a different type of orbit than OCO-2 and S5P, and thus does not consistently take co-located measurements with the instruments in sun-synchronous orbits. This can lead to much greater time differences between co-located OCO-3 and TROPOMI measurements compared to the differences between observations from OCO-2 and TROPOMI. Upon identifying a favorable OCO-3 overpass of a city, the TROPOMI track which lies closest to the city is selected. Time offsets are as large as 6 hours between observations from the two instruments. This leads to greater uncertainties in cases where the wind direction has changed significantly in the time between overpasses, as the regions that are affected by the city's plume may no longer coincide with one another.

Finding instances of co-located measurements of $NO_2$ and CO from TROPOMI is a far simpler task. Here we search for instances of measurements directly over each city of interest, leading to 1 or sometimes even 2 overpasses per day, depending on the longitude of the ground tracks. Due to this much higher data volume, only direct observation of the cities are considered when deriving $NO_2$:CO ratios to avoid including measurements which are not influenced by the cities due to wind direction errors.

### 3.2 Identifying Enhancements

To identify the subset of measurements which are influenced by emissions from the city, we transform the latitude-longitude positions of the observations into along- and cross-wind distances from the city centre and use the equation for the spread of a vertically-integrated Gaussian plume, defined by Krings et al. (2011) as

$$\sigma_y = a \left( \frac{x + x_0}{x_c} \right)^{0.894}, \tag{2}$$

where $x$ is the downwind distance in metres, $x_c = 1000$ m is a characteristic length scale and $a$ is the atmospheric stability parameter (Pasquill, 1961; Krings et al., 2011; Nassar et al., 2017, 2021) which controls the spread of the plume based on the observed MERRA-2 50 m wind speed, so that the plume changes width depending on the wind speed and insolation. Following Nassar et al. (2017), we use the Pasquill-Gifford stability class to determine the atmospheric stability parameter (Martin, 1976), and as in Nassar et al. (2021) we assume solar insolation to be strong given the clear-sky requirements for dense OCO-2/3 observation. The distance $x_0$ is used to define the initial width of the plume and is defined by

$$x_0 = x_c \left( \frac{y_0}{4a} \right)^{\frac{1}{0.894}}, \tag{3}$$

where $y_0$ is the cross-wind extent of the city in metres. The factor of 4 in the definition of $x_0$ follows the method of Krings et al. (2011) so that the cross-wind extent of the city is associated with a $\pm 2\sigma_y(x_0)$ spread of the plume. Downwind observations with cross-wind distances that are less than $2\sigma_y(x)$ from the mean path from the city $y$ are considered to be in the plume. In cases where the winds point parallel to the affected OCO-2 track, a maximum downwind distance for the plume is determined manually to limit the length of the plume to an area where significant enhancements are observed.

For comparisons between the TROPOMI $NO_2$ and CO products, where we do not consider a plume region, the enhancement area is taken as the bounding box of the GHS polygon for the city.

### 3.3 Anomaly Calculation

#### 3.3.1 Smoothing of Urban Influenced Data

To decrease the amount of noise in the OCO-2/3 and TROPOMI data, we apply a nearest neighbour fit with a constant radius to smooth out the data (Altman, 1992). For the narrow swath width of OCO-2, we find that fitting a surface to the OCO-2 time series and using a radius of 2 seconds leads to a fit that removes high frequency noise but retains the overall trends (Figure 1). Due to the wide swath width of TROPOMI, it is more appropriate to fit a spatial surface to the data. We find that using a radius of 15 km effectively smooths the data, and is comparable in spatial extent to the smoothing applied to the OCO-2 data. Fitting these surfaces to the datasets has the added advantage that predictions can be made at locations which do not have direct measurements, but have adequate nearby coverage. This lessens the impact of spurious missing data when trying to find co-located measurements.

### 3.3.2 Background Calculation

A regional background for $X_{CO_2}$ is determined using nearby measurements from OCO-2 that are free from anthropogenic influence. A nearest neighbour fit similar to that used to smooth the urban influenced data is applied here, but with a much larger radius of 20 seconds (approximately 140 km). This choice of radius creates a background whose extent is similar to those in the simulations performed by Wu et al. (2018). The background fit is performed using typically the lowest 75 percent of the retrievals, so that potential enhancements are removed. For some individual overpasses, the choice of percent must be tuned if the nearest neighbor background fit gives a trend that appears to be too high or too low compared to nearby observations which are unaffected by any urban plumes. The performance of this method appears to be most accurate when winds run perpendicular to the OCO-2 track and there exist dense soundings both prior to and after crossing the plume of the city, however satisfactory results were still found in cases where soundings were missing on one side of the plume, which is often the case when cities close to a body of water are observed in nadir mode. Figure 1 shows an example of the process of smoothing the data, identifying an enhancement, and calculating the background for an overpass of Moscow with OCO-2.

A similar method is used to define the background for TROPOMI. A radius of 150 km is used for this fit, again using only the lowest 75 percent of data to avoid the influence of anthropogenic enhancements on the background. Due to the larger swath width and generally more dense measurements of the TROPOMI products, we find the value does not need to be tuned from 75 percent for individual overpasses.

### 3.3.3 Calculation of Anomalies

Anomalies are calculated by subtracting the background estimates from the smoothed urban influenced values. Coincident observation locations are then chosen using the locations from the sparser of the two species being investigated. For example, if a ratio between CO and $CO_2$ is being determined, the observation locations from OCO-2 or OCO-3 are used, as their spatial coverage is much smaller than that of the TROPOMI CO product.

These anomalies are divided by the surface averaging kernel values, which is similar to the method used by Wunch et al. (2009) to account for the sensitivities of the instruments to changes in trace gas concentrations near the surface of the Earth, where the emissions from cities originate. Figure 2 demonstrates this anomaly calculation procedure, and Figure 3 shows an example of the distributions of surface averaging kernels for the three gases that are considered.

### 3.4 Determination of Enhancement Ratios

To determine enhancement ratios, we regress one set of anomalies onto the other using a reduced major axis regression as described by York et al. (2004), as shown in Figure 4. The variance of the samples is used as the uncertainty for each observation. Reduced major axis regression has the property that the resulting slope is independent of which variable is chosen to be on the abscissa and which is chosen to be on the ordinate axis. Furthermore, the calculated slope is unaffected by the scaling of axes by a constant value, so that the calculated slopes are independent of the choice of mixing ratio units that are used (i.e. ppm or ppb). This method is then bootstrapped (Efron and Gong, 1983) 500 times to get an error estimate for the fit. Bootstrapping
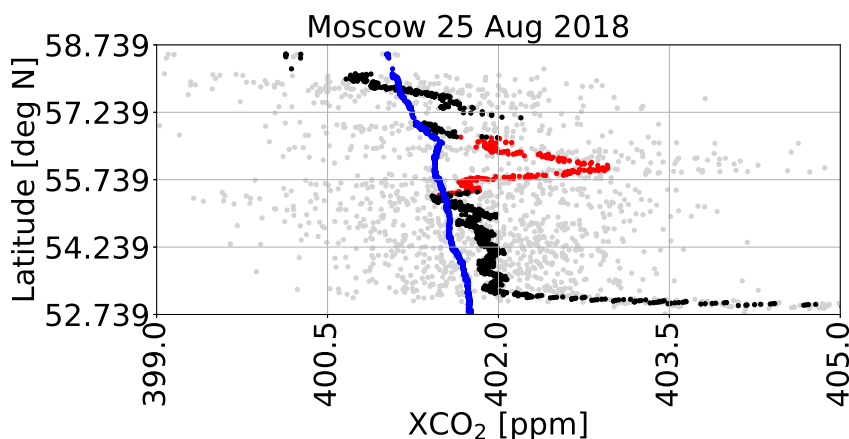
**Figure 1.** An example of of the background and anomaly calculation procedure for OCO-2 data over Moscow (Russia) on 25 August 2018. The grey points represent the original measurements from the OCO-2 Lite files. The black and red points indicate the smoothed data, with the red points corresponding to those in the urban enhancement plume of the city being investigated. The blue line shows the derived background using the lowest 75 percent of data.

is a re-sampling technique in which random samples of the same size as the original data are drawn with replacement and fit independently, and has been used in previous emissions ratio studies (e.g., Wunch et al., 2009, 2016; Lama et al., 2020). We take twice the standard deviation of the resulting set of slopes as the uncertainty estimate for the fit.

### 3.5 NO$_2$ Lifetime Correction

NO$_2$ has a short atmospheric lifetime compared to those of both CO$_2$ and CO, and can be on the same order as the advective time scales associated with emissions on the scale of large cities. To account for this, we apply a correction to the observed enhancement ratios to model the effect of NO$_2$ lifetime. Following Lutsch et al. (2020), the multiplicative correction takes the form

$$C = \exp\left(\tau_A / \tau_{\mathrm{NO_2}}\right), \tag{4}$$

where $\tau_A$ is a time scale for advection and $\tau_{NO_2}$ is the lifetime of NO$_2$. This uses the fact that the chemical loss of NO$_2$ can be modeled as $\mathrm{NO_{2,orig}} \cdot \exp(-t/\tau_{\mathrm{NO_2}})$. Thus, when $t = \tau_A$, the ratio of $\mathrm{NO_{2,orig}/NO_{2,downwind}} = C$. As we are correcting enhancement ratios, the effect of dispersion cancels out in the ratio. We use the method described in Laughner and Cohen (2019) to calculate NO$_2$ lifetimes for each city separately for summer and winter (details given in Appendix B). We apply a
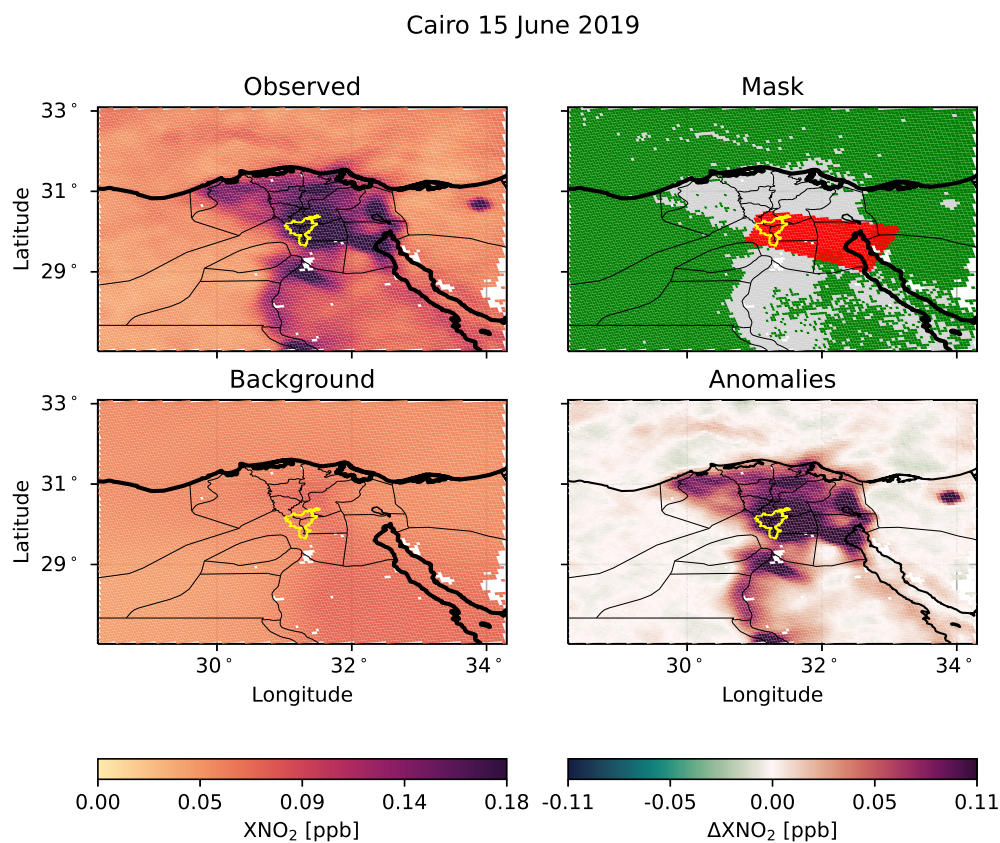
**Figure 2.** An example of the background and anomaly calculation procedure for TROPOMI $NO_2$ observations over Cairo on 15 June 2019. The top left panel shows the smoothed set of observations. The top right shows the mask for the background calculation; green points are used in the calculation while grey points are omitted, and red points indicate observations in the enhancement. The selection of the enhancement region is done liberally, as the location of OCO-2/3 observations is often a more limiting factor. The lower left panel then shows the derived background, and the lower right panel the calculated anomalies. The extent of the GHS polygon for Cairo is shown in yellow. Thick black lines mark coastlines, and thin black lines indicate geopolitical boundaries.
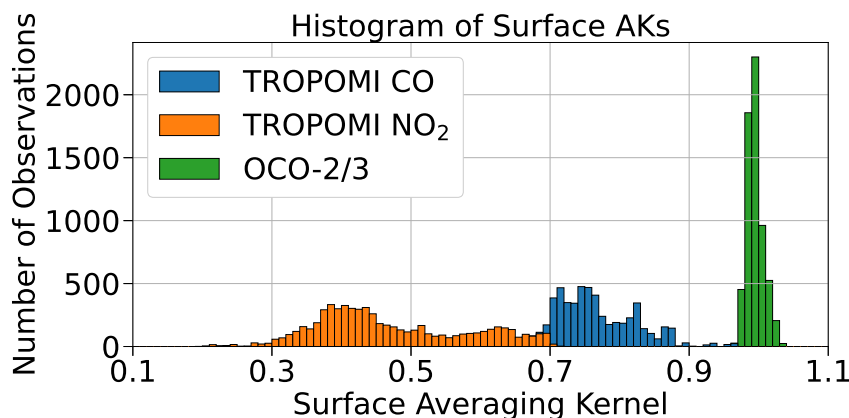
**Figure 3.** Example histograms of the surface level averaging kernel values for OCO-2/3 and TROPOMI from all the data collected over Phoenix (USA), which are used to account for the sensitivity of the instruments to concentration changes at the surface.
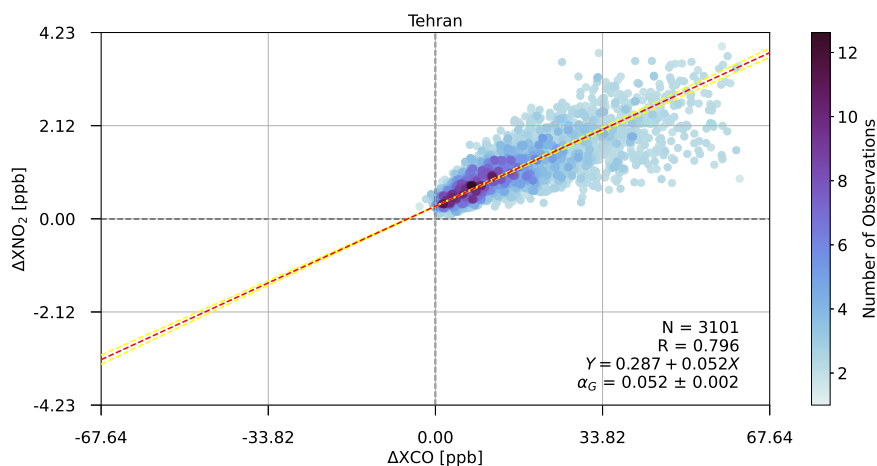
**Figure 4.** Regression of anomalies of $X_{NO_2}$ onto anomalies of $X_{CO}$ over Tehran using TROPOMI data from June–August 2018. The red dashed line indicates the estimated enhancement ratio, while the yellow lines represent $\pm 2\sigma$ uncertainties in the ratio. Each data point represents a single observation, and is assigned a color to indicate the density of points by binning the observations into 100 bins across each axis, and counting the number of points in the bin in which the observation resides. N is the total number of points included in the regression, R is the correlation coefficient, Y is the equation of best fit, and $\alpha_G$ is the slope and $2\sigma$ uncertainty determined by bootstrapping.

single lifetime correction by scaling the observed enhancement ratio so that $\alpha_{\text{Corrected}} = C\alpha$, with an advection time scale given by

$$\tau_A = \frac{1}{\overline{U}} \left( \frac{A}{\pi} \right)^{1/2},\tag{5}$$

290 where $\overline{U}$ is the average wind speed averaged across all overpasses of the city and weighted by the number of observations in each overpass, and $A$ is the area of the city provided in GHS-UCDB so that the relevant length scale is the radius of the city if it were perfectly circular. In applying these corrections, we have neglected the lifetimes of CO and $CO_2$, which are on the order of months and centuries, respectively, and therefore will have a negligible effect on the observed enhancement ratios. To account for errors in the $NO_2$ lifetimes as well as the wind speeds used to calculate the advective time scales, we prescribe an

295 additional uncertainty of 20% to the enhancement ratios when the lifetime correction is applied.

## 4 Results

### 4.1 $NO_2$:$CO_2$ and CO:$CO_2$ Ratios

Using these methods, we are able to quantify $NO_2$:$CO_2$ ratios from 21 cities, and CO:$CO_2$ ratios from 20 cities using co-located observations from TROPOMI, OCO-2 and OCO-3. A total of 162 overpasses occurring from April 2018 to May 2020

300 are used to derive $NO_2$:$CO_2$ ratios, with 135 consisting of observations from TROPOMI and OCO-2, and the remaining 27 involving TROPOMI and OCO-3. The most overpasses for an individual city are found for Phoenix (United States), where we found 20 usable overpasses; Toronto has the fewest, where only a single overpass is used. In many cases, overpasses involving OCO-3 had to be filtered out due to observed non-linear relations between the derived $X_{CO_2}$ anomalies and those from the two TROPOMI products for a given day. This issue is most likely caused by the greater time differences between overpasses

305 of the ISS and S5P—the location and distribution of the plumes could change significantly between the two times at which measurements are made so that the measurements are no longer approximately co-located in time and space.

Cities located in the Southwestern United States (Los Angeles, San Francisco, Phoenix, and Las Vegas) and in the Middle East (Tehran, Baghdad, and Cairo), generally yielded more usable overpasses than cities located elsewhere in the world due to the greater number of cloud-free daylight hours in these regions. Few good overpasses were found for cities located in

310 East and Southeast Asia, as observations from OCO-2/3 are often very sparse due to persistent clouds; other than Guangzhou (China) and Seoul (South Korea), megacities in these regions of the globe are not considered in this study. Overpasses were also generally better for inland cities compared to those situated next to large bodies of water, where loss of data from nadir viewing in the OCO-2/3 product and data filtering the TROPOMI CO product led to more limited opportunities to make observations downwind of the city. The presence of mountains near cities also presented some problems; in such cases large corrections to

315 the reported MERRA-2 wind directions were often required to properly capture the plume. In the unique case of Los Angeles and the SoCAB in which the city resides, we considered only measurements directly above the SoCAB in our analysis, as the surrounding mountain ranges prevent air from easily leaving the basin.
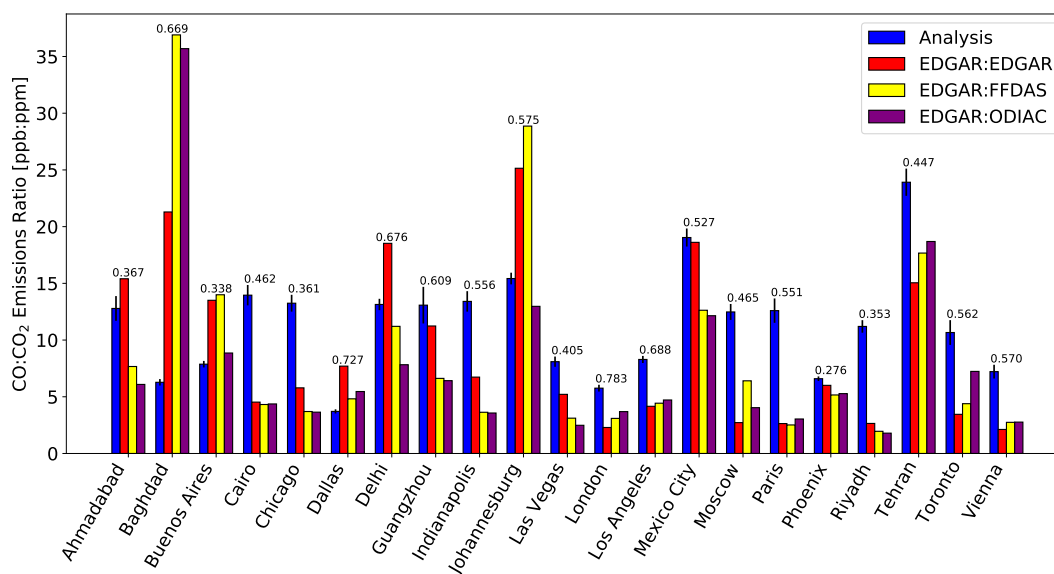
**Figure 5.** $CO:CO_2$ enhancement ratios derived using observations from OCO-2/3 and TROPOMI compared to inventory estimates using CO emissions from EDGAR and $CO_2$ emissions from EDGAR, FFDAS and ODIAC. The numbers on top of the bars denote the correlation coefficient between the two sets of observed anomalies. The light blue areas atop the bars represent the uncertainty in the measured ratios.

Figure 5 shows the derived $CO:CO_2$ enhancement ratios from our analysis compared to inventory based estimates of the enhancement ratios derived from the ODIAC, FFDAS and EDGAR emissions inventories. For cities across the United States,

320 Canada, and Europe, we find that apart from the Dallas-Fort Worth area, our measured enhancement ratios are higher than the inventory-based estimates, with our results ranging from around 1.1 (Phoenix) to 4.8 (Paris) times greater than the respective EDGAR estimates. Results for the remainder of the cities show a less consistent picture, with the largest underestimate being for Baghdad (Iraq), where we find an enhancement ratio that is around 3 times lower than that of the EDGAR estimate, and the largest overestimate for Tehran, where the measured enhancement ratio is around 1.6 times greater than the EDGAR value.

325 When comparing to ratios calculated using CO emissions from the MACCity inventory, shown in Appendix A, we find a more pronounced underestimation compared to observations across North America and Europe.

Figure 6 similarly shows results for the derived $NO_2:CO_2$ ratios, both with the correction for $NO_2$ lifetime and without. Here we find that without any $NO_2$ lifetime correction, almost all of the cities considered have derived ratios that are smaller than the inventory-based estimates. As with the $CO:CO_2$ results, this discrepancy is most pronounced in the United States

330 and Europe. Upon applying our lifetime correction to the ratios, the ratios in many of these cities are brought closer to the inventory-based estimates, with a few cities (Delhi, Johannesburg, Mexico City and Tehran) having ratios that are higher than any of the inventory estimates. Additionally, correlation coefficients between the two sets of anomalies were generally found to be greater in this case when compared to the $CO:CO_2$ enhancement ratios results. Ratios calculated using the MACCity
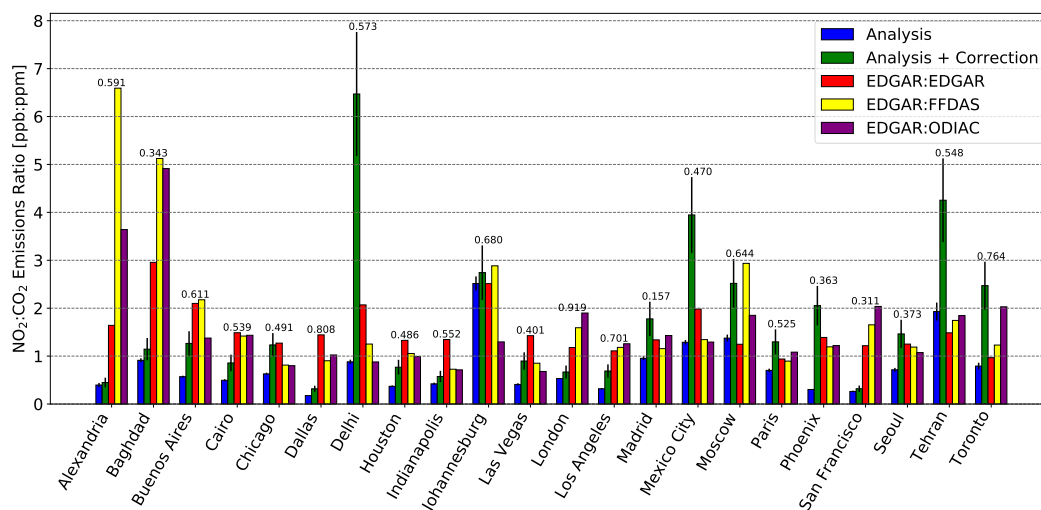
**Figure 6.** Same as in Figure 5 but for $NO_2$:$CO_2$ ratios derived using OCO-2/3 and TROPOMI observations. $NO_2$ enhancements are calculated without a lifetime correction in blue, and with a lifetime correction in green.

inventory, shown in Appendix A, show better agreement with those derived using satellite observations prior to the application

335 of the lifetime correction, but observed enhancements are generally higher than the inventory estimates after the atmospheric lifetime correction is applied.

## 4.2 NO$_2$:CO Ratios

We also derive $NO_2$:CO ratios for the same cities using only measurements from TROPOMI. Because $NO_2$:CO enhancement ratios do not use observations from OCO-2/3 which have more limited coverage, there are far more opportunities for calculating

340 these ratios. In the absence of cloud cover, we obtain 1–2 overpasses per day for each city. We consider a smaller subset of the TROPOMI product from June–August 2018, which is the same subset of data used by Lama et al. (2020), so that our enhancement ratios are derived from 40–100 overpasses for each city. Because there are more overpasses averaged into the $NO_2$:CO estimates of enhancement ratios, we expect them to be more robust than those involving OCO-2/3.

Figure 7 shows the derived $NO_2$:CO ratios compared to inventory-based estimates from EDGAR and MACCity. Here we

345 observe ratios that are significantly lower than inventory-based estimates both before and after the lifetime correction has been applied. Again these differences are generally more significant over cities in North America and Europe, and Johannesburg and Baghdad are outliers, with observed enhancement ratios higher than either of the inventory estimates. Table 2 summarizes the results of all three sets of emissions ratios for all the cities considered.

We also compare our $NO_2$:CO results to those of Lama et al. (2020), where two different methods were used to calculate

350 $NO_2$:CO enhancement ratios in six megacities (Tehran, Mexico City, Cairo, Riyadh, Lahore and Los Angeles) using measure-
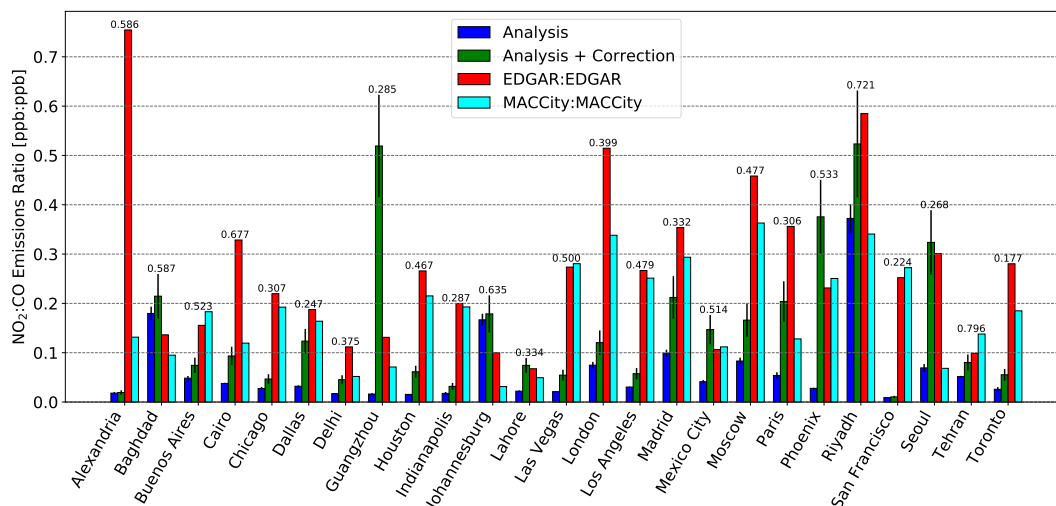
**Figure 7.** Same as in Figure 5 but for $NO_2$:CO ratios derived using observations from TROPOMI. EDGAR and MACCity are used to calculate inventory-based estimates of the emissions ratios.

ments from TROPOMI. Lama et al. also use an averaging kernel correction to their ratios, except with a different methodology; they apply column averaging kernels to reported profiles of $NO_2$ and CO from the Copernicus Atmospheric Monitoring Service (CAMS) to determine the impact on $X_{NO_2}$ and $X_{CO}$. Lama et al. also apply a correction which accounts for the short lifetime of $NO_2$ due to chemical reactions with hydroxyl (OH) in the atmosphere by constructing a correcting scale factor

355 using CAMS-reported OH concentrations and the observed wind speed. Comparing the results of Lama et al. (2020) to our calculated values without their respective $NO_2$ lifetime corrections, we find good agreement in the ratios for Tehran, Mexico City, Cairo and Los Angeles, with ratios agreeing to within 25% of each other. Larger discrepancies are observed for Riyadh and Lahore, where we find ratios significantly higher than those of Lama et al., by factors of around 3.5 and 2, respectively. These differences may be influenced by the different averaging kernel corrections used, as the corrections used in Lama et al.

360 are derived from averaging kernels and CAMS data over Riyadh and Lahore for a limited number of days, while our correction uses averaging kernels from each overpass of the city. After the application of the respective $NO_2$ lifetime corrections, the results for Mexico City and Los Angeles still demonstrate good agreement; enhancement ratios for these two cities agree to within 15%. For Tehran and Cairo the agreement has been degraded, as the $NO_2$ lifetime correction of Lama et al. (2020) is around twice the magnitude of our correction for these two cities.

## 5 Discussion

### 5.1 Analysis of Measured Ratios

The $CO:CO_2$ ratios that we derive using TROPOMI and OCO-2/3 are larger than the inventory-based estimates calculated from EDGAR, ODIAC, and FFDAS in 70% of the cities we studied (Figure 5). This is the case for nearly all cities in North America and Europe, though mixed results are observed for the rest of the world; in cities such as Tehran (Iran) and Cairo (Egypt) we observe high ratios relative to inventory estimates, while in Johannesburg (South Africa), Baghdad (Iraq) and Buenos Aires (Argentina), we observe ratios that are lower than the inventory values. We also observe larger $CO:CO_2$ enhancement ratios relative to reported emissions ratios when using CO emissions from the MACCity inventory (Figure A1). Here, the low bias for inventory estimates appears to be even stronger for cities in North America and Europe, while Johannesburg and Baghdad remain as outliers with lower observed enhancement ratios.

For the $NO_2:CO_2$ ratios that we calculate (Figure 6), we find that without any correction for $NO_2$ lifetime, this trend is reversed: we observe ratios that are considerably lower than those derived from EDGAR, ODIAC and FFDAS in 77% of the cities. Upon application of our correction for $NO_2$ lifetime, the ratios for many of these cities are brought in closer agreement with the inventory estimates. Los Angeles is the city most affected by the addition of the lifetime correction, with its ratio increasing by a factor of around 3. Johannesburg is a notable outlier, with an observed ratio that is comparable to the EDGAR and FFDAS estimates, yet is around twice the EDGAR:ODIAC estimated ratio before correction, and higher than all three emission ratios after correction. Delhi, Mexico City and Tehran also have ratios that exceed inventory-based estimates by a similar amount after the lifetime correction has been applied. An added complication for the specific case of Johannesburg is the presence of a collection of large coal-fired power plants located ~100 km east of the city which together emit > 10 $TgCO_2$/yr and an additional two power plants located ~50 km to the south according to the Carbon Monitoring for Action (CARMA) database (Ummel, 2012). Plumes from these sites are clearly visible in CO and $NO_2$ measurements from TROPOMI and depending on the wind direction and distance from the city could influence the measurements in the OCO-2 swath. Interestingly, the positions of these four cities (Delhi, Johannesburg, Mexico City, Tehran) as outliers appears to be consistent for both EDGAR $NO_x$ emissions and those from MACCity.

In general, we find that measured $NO_2 : CO$ enhancement ratios are smaller than those inferred from the inventories, while measured $CO : CO_2$ ratios are generally larger. Measured $NO_2 : CO_2$ ratios are generally in good agreement with the inferred inventory enhancement ratios. From our observed $CO:CO_2$ ratios, which are generally larger than the inventory ratios, we infer that the inventories we considered tend to either underestimate CO emissions, overestimate emissions of $CO_2$, or both. Similarly, the $NO_2:CO_2$ ratios that are observed to generally agree with the EDGAR $NO_x$-based estimates suggests that either the inventories accurately capture emissions of both $NO_2$ and $CO_2$, or that emissions of these two gases are both biased either high or low by a similar magnitude. Given that the spread provided by the three $CO_2$ inventories (which is on average about 20% around the mean of the three, and exceeds 30% for only Alexandria, Delhi, Johannesburg and Moscow) coincides with the uncertainty range for the $NO_2:CO_2$ enhancement ratio in 8 out of 22 cities, and is close for another 7 cities, the $NO_2:CO_2$ emissions ratios do not appear to be affected by systematic biases as much as the $CO:CO_2$ ratios. From this, we infer that the

discrepancies in the $NO_2$:CO ratios are likely caused by an underestimation of CO emissions within the EDGAR inventory.
400 A similar picture emerges for the MACCity $NO_2$:CO ratios using figures A1 and A2. Here, the high $NO_2$:CO ratios (yellow bars in Figure 7) relative to observations seem to be driven by an even stronger underestimation of CO emissions.

If we were to rescale the CO inventory emissions so that their emissions ratios matched the observed $CO : CO_2$ enhancement ratios, EDGAR CO emissions would have to be about doubled on average. For MACCity, the required rescaling factor is considerably higher; this was driven in part by severely low-biased CO emissions estimates in Riyadh (Saudi Arabia), Las
405 Vegas (USA) and Phoenix (USA). This suggests that MACCity may systematically underestimate CO emissions in desert cities. Even when neglecting these three cities, the low-biased emissions in MACCity would still require a rescaling factor of around 4 on average to match the observed enhancement ratios.

### 5.2 Emissions Estimates using High-Resolution Inventories

In addition to the global, gridded inventories that we have employed up to this point, the cities of Indianapolis (USA) and Los
410 Angeles (USA) also have high-resolution anthropogenic $CO_2$ inventories. The Hestia Inventory provides gridded fluxes for the cities of Los Angeles, Indianapolis, Salt Lake City and Baltimore at both hourly and annual temporal resolutions for the years 2010–2015 (Gurney et al., 2018b, 2019). The inventory for Los Angeles is provided at a spatial resolution of 1 km × 1 km for the SoCAB and the surrounding area, and the inventory for Indianapolis is given on a 200 m × 200 m grid. When summed across the GHS polygons for each city, the annual emissions for Los Angeles and Indianapolis from the Hestia inventory are
415 120.9 $TgCO_2$/yr and 13.5 $TgCO_2$/yr, respectively. For Los Angeles, the annual estimates of the global gridded inventories (EDGAR, ODIAC, and FFDAS) are between 25-33% lower than this high resolution estimate, while for Indianapolis, the Hestia estimate is similar to the mean of the three global inventories. When comparing with the TIMES-corrected emissions rates from the global inventories for Los Angeles, the estimates are brought into better agreement with the Hestia inventory, with emissions rates that are now only 6-17% lower than Hestia. For Indianapolis, the TIMES-corrected EDGAR estimate of
420 9.5 $TgCO_2$/yr is about 30% lower than the Hestia estimate, while the ODIAC and FFDAS values are around 30% higher.

Using the $CO:CO_2$ enhancement ratio that was calculated for Los Angeles along with the Hestia emissions estimate and equation 1, we estimate CO emissions to be $638 \pm 130$ GgCO/yr after assuming a 20% uncertainty in the Hestia emissions estimate, which has good overlap with the estimate of $487 \pm 122$ GgCO/yr found by Hedelius et al. (2018) for 2013–2016, as well as the value of 581 GgCO/yr for the SoCAB which is reported by the California Air Resources Board (CARB) for the
425 year 2015 in the CARB2017 database (https://www.arb.ca.gov/app/emsinv/2017/emssumcat.php). In a similar way we estimate emissions of $NO_2$ within the SoCAB to be $40 \pm 8$ $GgNO_2$/yr, which is around 68% lower than the CARB estimate for 2015 of 105 $GgNO_2$/yr. After applying the $NO_2$ lifetime correction, the estimate is increased to $149 \pm 42$ $GgNO_2$/yr, bringing it closer into agreement with the CARB estimate for 2015 and the annual EDGAR estimate of 132 $GgNO_2$/yr, but far greater than the MACCity estimate of 43.3 $GgNO_2$/yr. CARB2017 projections for the year 2020 estimate that SoCAB emissions of
430 CO and $NO_x$ should decrease by 21% and 26% respectively.

A similar approach using the Hestia $CO_2$ Inventory for Indianapolis yields estimated CO emissions of $115 \pm 24$ GgCO/yr, much higher than both the EDGAR and MACCity estimates of 40.7 GgCO/yr and 11.7 GgCO, respectively. Using the un-

corrected $NO_2$:$CO_2$ ratio, emissions of $NO_2$ are estimated to be $6.0 \pm 1.3$ Gg$NO_2$/yr; application of the correction gives
an estimate of $10.5 \pm 3.0$ Gg$NO_2$/yr, which is considerably higher than the MACCity estimate of 3.9 Gg $NO_2$/yr, but has an
435  uncertainty range that covers the EDGAR estimate of 13.4 Gg$NO_2$/yr. These investigations of Los Angeles and Indianapolis il-
lustrate how the high MACCity $NO_2$:CO ratios observed in Figure 7 are driven by a strong underestimation of CO emissions,
even though the $NO_x$ emissions are also underestimated in MACCity compared to the estimate derived from enhancement
ratios and Hestia.

## 6  Conclusions

440  This study demonstrates a method to derive enhancement ratios between $CO_2$, CO and $NO_2$ using measurements from the
OCO-2, OCO-3, and TROPOMI satellite instruments located downwind of or over large urban areas. This method is applied to
derive enhancement ratios for 27 cities from around the world. These ratios are then compared to enhancement ratios derived
from the EDGAR, ODIAC, FFDAS, and MACCity global inventories. We find that CO:$CO_2$ ratios from these inventories are
generally lower in cities across Europe and North America compared to the satellite-based ratios. After applying a correction
445  to account for the short atmospheric lifetime of $NO_2$, observed $NO_2$:$CO_2$ ratios are mostly higher than inventory ratios when
using $NO_x$ emissions from MACCity but generally show good agreement when using emissions from EDGAR, apart from a
few outlier cities where observed ratios were high compared to inventory estimates. $NO_2$:CO ratios retrieved from TROPOMI
observations over these cities show low values relative to inventory estimates and good agreement with the $NO_2$ : CO ratios
derived in a previous study by Lama et al. (2020).

450      We demonstrate that deriving enhancement ratios between more than two species can aid in the interpretation of results. By
measuring ratios of CO:$CO_2$, $NO_2$:$CO_2$, and $NO_2$:CO, we are able to better diagnose which emissions lead to discrepancies
between satellite- and inventory-derived ratios. For the EDGAR inventory, this analysis suggests an underestimation of CO
emissions by around 50% on average, while for the MACCity inventory, we infer a more significant underestimation of CO
emissions of about 75% on average, alongside a smaller underestimation of $NO_x$ emissions. In both EDGAR and MACCity,
455  many of the largest underestimations are observed for cities in Europe and North America, with MACCity showing significant
underestimation in desert cities (Riyadh, Phoenix, Las Vegas). Further, we show that by combining these enhancement ratios
with high-resolution $CO_2$ inventories, emissions of CO and $NO_2$ can be calculated, which, in the case of Los Angeles, show
good agreement with both region-specific inventories and previous modelling studies. These analyses with high-resolution
inventories additionally provide further support for the underestimation of urban CO emissions in EDGAR and MACCity.

460      There is considerable potential for further study using the methodology that has been laid out here. In particular, these
methods could be applied to other anthropogenic co-emitters of $CO_2$, CO and $NO_2$. Fossil fuel burning power plants are a
candidate for future investigations, as other studies have already used multi-sensor techniques involving $NO_2$ and $CO_2$ to
estimate power plant emissions (e.g., Reuter et al., 2019; Hakkarainen et al., 2021). Furthermore, enhancement ratios involving
other species are observed by TROPOMI, such as $CH_4$, HCHO, and $SO_2$ over urban regions could be explored using the
465  framework that has been described here.

Due to the limited number of usable co-locations between OCO-2/3 and TROPOMI that were available in this study, we have limited our enhancement ratio results to single values across the full time periods. As the constellation of $CO_2$ observing satellites expands in the coming years, there will be greater potential for co-locations of observations, which could provide reliable information on long-term trends of these enhancement ratios and open up the possibility for comparison to trends
470 in ratios derived from emissions inventories. When paired with state-of-the-art $CO_2$ inventories, these enhancement ratios could provide a flexible framework to determine whether emissions reduction targets for a wide array of greenhouse gases and pollutants are being met on schedule by cities around the world.

*Data availability.* OCO-2 and OCO-3 data were obtained from the Goddard DAAC https://disc.gsfc.nasa.gov/datasets/OCO2_L2_Lite_FP_ 9r/summary, https://disc.gsfc.nasa.gov/datasets/OCO3_L2_Lite_FP_10.4r/summary?keywords=OCO-3%20vEarly. TROPOMI data were ob-
475 tained from the NASA GES DISC (CO: https://tropomi.gesdisc.eosdis.nasa.gov/data/S5P_TROPOMI_Level2/S5P_L2__CO_____.1 and $NO_2$: https://tropomi.gesdisc.eosdis.nasa.gov/data/S5P_TROPOMI_Level2/S5P_L2__NO2_____HiR.1/. TROPOMI $NO_2$ data for the lifetime calculation was obtained from the Sentinel-5P hub (https://s5phub.copernicus.eu/dhus/). GHS-UCDB is available from https://data.europa. eu/doi/10.2760/037310. ODIAC2020 is available from http://doi.org/10.17595/20170411.001. FFDAS2.2 is available from http://ffdas.rc. nau.edu/Data.html. TIMES is available from https://cdiac.ess-dive.lbl.gov/ftp/Nassar_Emissions_Scale_Factors/... EDGAR5.0 is available
480 from https://edgar.jrc.ec.europa.eu/dataset_ghg50. MACCity is available from http://accent.aero.jussieu.fr/MACC_metadata.php. MERRA-2 data are available from https://gmao.gsfc.nasa.gov/reanalysis/MERRA-2/. Hestia data are available from https://catalog.data.gov/dataset/ hestia-fossil-fuel-carbon-dioxide-emissions-inventory-for-urban-regions-82c05.

## Appendix A:  Comparison of CO:$CO_2$ and $NO_2$:$CO_2$ ratios with emission ratios derived from MACCity

Comparison of our observed CO:$CO_2$ enhancement ratios with emission ratios calculated using CO emissions from the MAC-
485 City inventory are shown in Figure A1. Results are similar to those using the EDGAR CO emissions, with underestimation by the inventories relative to the observations even more pronounced for many cities in Europe and North America. Similarly, Figure A2 shows a comparison of observed $NO_2$:$CO_2$ with MACCity derived emissions ratios. These emission ratios are characterized by a greater underestimation relative to the observed enhancement ratios when compared with the EDGAR emissions. As with the EDGAR emissions ratios, the cities of Delhi, Johannesburg, Mexico City and Tehran stand out as the
490 cases where this underestimation is the most pronounced.

## Appendix B:  $NO_2$ lifetime calculation

We compute $NO_2$ lifetimes similarly to Laughner and Cohen (2019) using $NO_2$ column densities from offline TROPOMI data (processor version 1.3). Wind direction for each day is calculated from GEOS-5 FP-IT reanalysis data (Lucchesi, 2015) by interpolating the bottom five levels of the wind fields to 13:30 local time. Horizontal averaging uses a flat topped Gaussian
495 (fourth power) centered on each city, with a width chosen based on the city size. $NO_2$ column densities from each day are
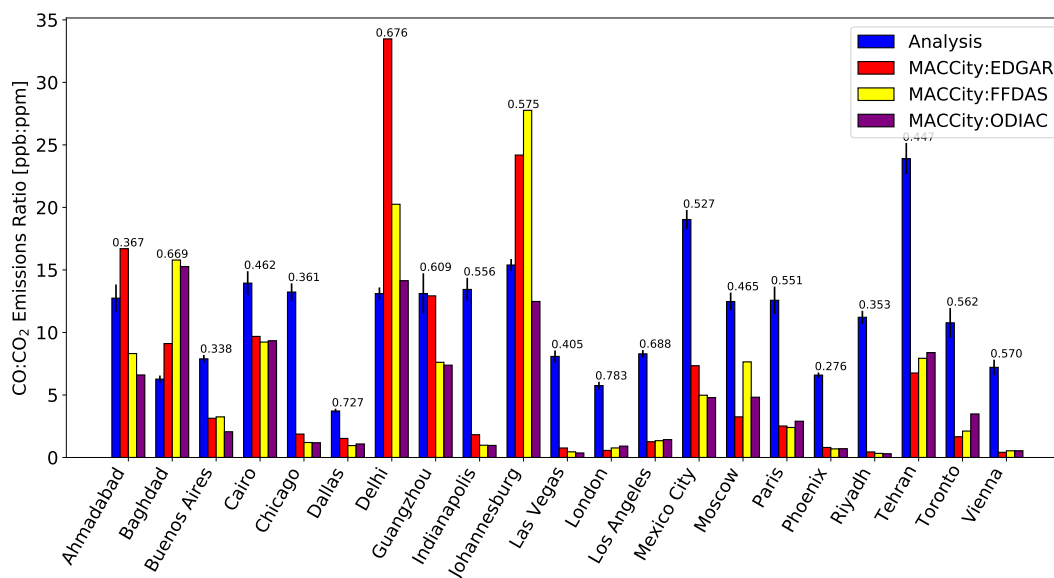
**Figure A1.** Same as is Figure 5 but for enhancement ratios calculated using CO emissions from the MACCity inventory.
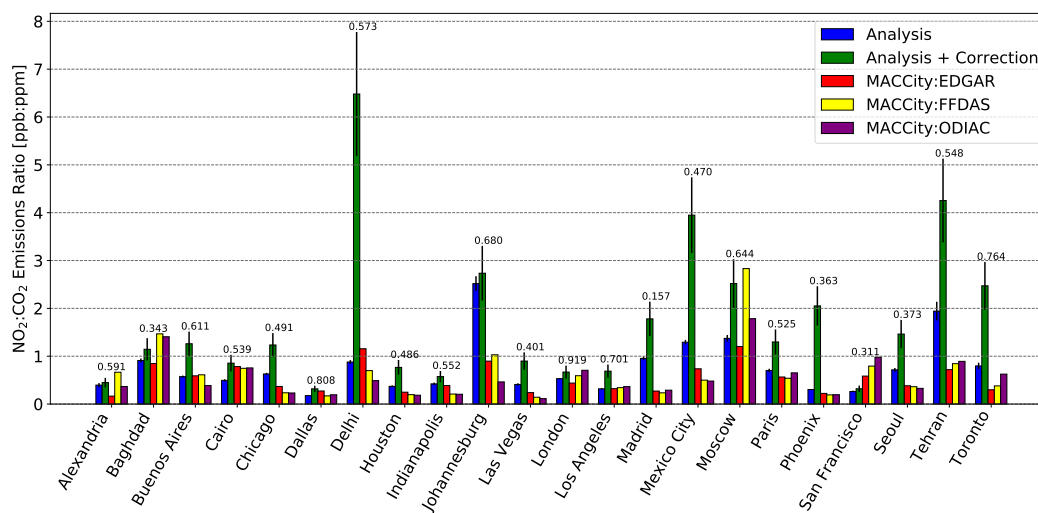
**Figure A2.** Same as in Figure 6 but for enhancement ratios calculated using $NO_x$ emissions from the MACCity inventory.

rotated so that the wind directions are aligned, and pixels with `qa_value` $> 0.75$ are averaged in time, weighted by the pixel

area. Line densities are computed by integrating the rotated line densities perpendicular to the wind direction. An exponentially-
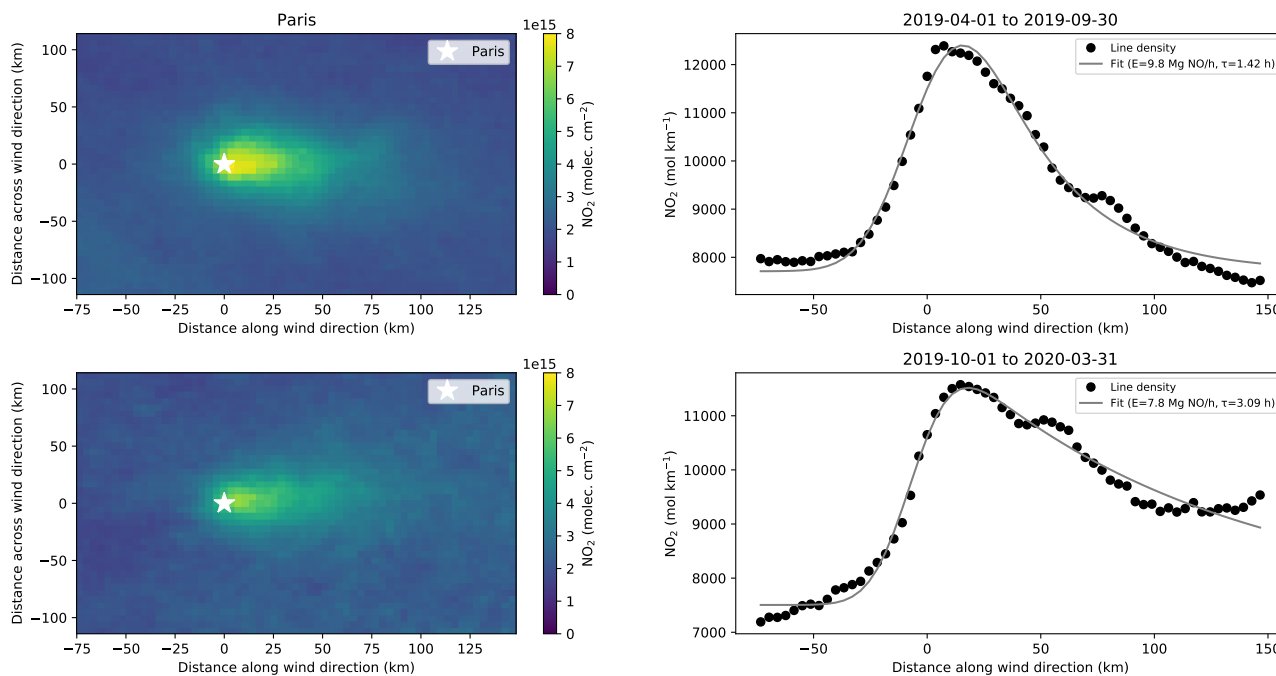
**Figure B1.** Example of lifetime fitting using Paris as a demonstration. The top row shows summer fits and the bottom row winter fits, with the specific dates used given in the title of the right panels. The left columns show the average $NO_2$ column density after aligning wind direction (right = downwind). The right columns show the line densities (black circles) and fits (grey lines) computed from the wind-aligned column densities.

modified Gaussian function,

$$F(x|a,x_0,\mu_x,\sigma_x,B) = \frac{a}{2x_0}\exp\left(\frac{\mu_x}{x_0} + \frac{\sigma_x^2}{2x_0^2} - \frac{x}{x_0}\right)\mathrm{erfc}\left(-\frac{1}{\sqrt{2}}\left[\frac{x-\mu_x}{\sigma_x} - \frac{\sigma_x}{x_0}\right]\right) \tag{B1}$$

500   is fit to the line densities. $x$ is the along wind distance and $a$, $x_0$, $\mu_x$, $\sigma_x$, and $B$ are fitting parameters. $\mathrm{erfc}$ is the error function complement. Lifetime is calculated as $x_0/\overline{u}$, where $\overline{u}$ is the average wind speed from GEOS FP-IT.

*Author contributions.* CGM designed the study, performed data analysis and wrote the manuscript. DW provided guidance across all stages of the process. JKH and RN supplied code which became part of the data analysis for the study and, with JPM, provided feedback during the writing of the manuscript. JLL computed the TROPOMI-derived $NO_2$ lifetimes and provided advice on their use, and feedback on the
505   manuscript.

*Competing interests.* We declare that we have no competing interests.

*Acknowledgements.* This project is undertaken with the financial support of the Canadian Space Agency as part of the Earth System Science Data Analyses Program, Grant #16SUASCOBF.

The authors gratefully acknowledge the efforts of the OCO-2, OCO-3, TROPOMI, EDGAR, ODIAC, FFDAS, MACCity, and Hestia
510 teams for producing these valuable datasets. OCO-2 and OCO-3 data were produced by the OCO-2 and OCO-3 projects at the Jet Propulsion Laboratory, California Institute of Technology. A portion of this research was carried out at the Jet Propulsion Laboratory, California Institute of Technology, under a contract with the National Aeronautics and Space Administration (80NM0018D0004).

# References

Altman, N. S.: An introduction to kernel and nearest-neighbor nonparametric regression, The American Statistician, 46, 175–185, 1992.

Asefi-Najafabady, S., Rayner, P., Gurney, K., McRobert, A., Song, Y., Coltin, K., Huang, J., Elvidge, C., and Baugh, K.: A multiyear, global gridded fossil fuel $CO_2$ emission data product: Evaluation and analysis of results, Journal of Geophysical Research: Atmospheres, 119, 10–213, 2014.

Borsdorff, T., Aan de Brugh, J., Hu, H., Hasekamp, O., Sussmann, R., Rettinger, M., Hase, F., Gross, J., Schneider, M., García Rodríguez, O. E., et al.: Mapping carbon monoxide pollution from space down to city scales with daily global coverage, Atmospheric Measurement Techniques (AMT), 11, 5507–5518, 2018.

Borsdorff, T., Schneider, A., Lorente, A., Birk, M., Wagner, G., Kivi, R., Hase, F., Feist, D. G., Sussmann, R., Rettinger, M., et al.: Improving the TROPOMI CO data product: update of the spectroscopic database and destriping of single orbits, Atmospheric Measurement Techniques, 12, 5443–5455, 2019.

Corbane, C., Florczyk, A., Pesaresi, M., Politis, P., and Syrris, V.: GHS built-up grid, derived from Landsat, multitemporal (1975-1990-2000-2014), R2018A, European Commission, Joint Research Centre (JRC). doi, 10, 2018.

Crippa, M., Solazzo, E., Huang, G., Guizzardi, D., Koffi, E., Muntean, M., Schieberle, C., Friedrich, R., and Janssens-Maenhout, G.: High resolution temporal profiles in the Emissions Database for Global Atmospheric Research, Scientific Data, 7, 121, https://doi.org/10.1038/s41597-020-0462-2, https://doi.org/10.1038/s41597-020-0462-2, 2020.

Crisp, D., Atlas, R., Breon, F.-M., Brown, L., Burrows, J., Ciais, P., Connor, B., Doney, S., Fung, I., Jacob, D., et al.: The orbiting carbon observatory (OCO) mission, Advances in Space Research, 34, 700–709, 2004.

Crisp, D., Pollock, H. R., Rosenberg, R., Chapsky, L., Lee, R. A., Oyafuso, F. A., Frankenberg, C., O'Dell, C. W., Bruegge, C. J., Doran, G. B., et al.: The on-orbit performance of the Orbiting Carbon Observatory-2 (OCO-2) instrument and its radiometrically calibrated products, Atmospheric Measurement Techniques, 10, 59–81, 2017.

Duren, R. M. and Miller, C. E.: Measuring the carbon emissions of megacities, Nature Climate Change, 2, 560–562, 2012.

Efron, B. and Gong, G.: A leisurely look at the bootstrap, the jackknife, and cross-validation, The American Statistician, 37, 36–48, 1983.

Eldering, A., Taylor, T. E., O'Dell, C. W., and Pavlick, R.: The OCO-3 mission: measurement objectives and expected performance based on 1 year of simulated data., Atmospheric Measurement Techniques, 12, 2019.

Eskes, H., van Geffen, J., Boersma, F., Eichmann, K., Apituley, A., Pedergnana, M., Sneep, M., Veefkind, J., and Loyola, D.: Sentinel-5 precursor/TROPOMI Level 2 Product User Manual Nitrogendioxide, Ministry of Infrastructure and Water Management, 2019.

European Commission and Joint Research Centre, Monforti-Ferrario, F., Oreggioni, G., Schaaf, E., Guizzardi, D., Olivier, J., Solazzo, E., Lo Vullo, E., Crippa, M., Muntean, M., and Vignati, E.: Fossil $CO_2$ and GHG emissions of all world countries : 2019 report, Publications Office, https://doi.org/doi/10.2760/687800, 2019.

Florczyk, A., Melchiorri, M., Corbane, C., Schiavina, M., Maffenini, M., Pesaresi, M., Politis, P., Sabo, S., Freire, S., Ehrlich, D., et al.: Description of the GHS Urban Centre Database 2015, Public Release, 2019.

Granier, C., Bessagnet, B., Bond, T., D'Angiola, A., van Der Gon, H. D., Frost, G. J., Heil, A., Kaiser, J. W., Kinne, S., Klimont, Z., et al.: Evolution of anthropogenic and biomass burning emissions of air pollutants at global and regional scales during the 1980–2010 period, Climatic Change, 109, 163, 2011.

Gurney, K., Romero-Lankao, P., Pincetl, S., Betsill, M., Chester, M., Creutzig, F., and Schäfer, K.: Chapter 4: Understanding urban carbon fluxes, Second state of the carbon cycle report (SOCCR2): A sustained assessment report, pp. 189–228, 2018a.

550   Gurney, K. R., Razlivanov, I., Song, Y., Zhou, Y., Benes, B., and Abdul-Massih, M.: Quantification of fossil fuel CO2 emissions on the
        building/street scale for a large US city, Environmental science & technology, 46, 12 194–12 202, 2012.

      Gurney, K. R., Liang, J., Yuyu, Z., Bedrich, B., and Patarasuk, R.: Hestia Fossil Fuel Carbon Dioxide Emissions Inventory for Urban Regions,
        https://doi.org/10.18434/T4/1502499, 2018b.

      Gurney, K. R., Liang, J., O'Keeffe, D., Patarasuk, R., Hutchins, M., Huang, J., Rao, P., and Song, Y.: Comparison of Global Downscaled Ver-
555     sus Bottom-Up Fossil Fuel CO2 Emissions at the Urban Scale in Four U.S. Urban Areas, Journal of Geophysical Research: Atmospheres,
        124, 2823–2840, https://doi.org/10.1029/2018JD028859, https://agupubs.onlinelibrary.wiley.com/doi/abs/10.1029/2018JD028859, 2019.

      Hakkarainen, J., Szeląg, M. E., Ialongo, I., Retscher, C., Oda, T., and Crisp, D.: Analyzing nitrogen oxides to carbon
        dioxide emission ratios from space: A case study of Matimba Power Station in South Africa, Atmospheric Environ-
        ment: X, 10, 100 110, https://doi.org/https://doi.org/10.1016/j.aeaoa.2021.100110, https://www.sciencedirect.com/science/article/pii/
560     S2590162121000101, 2021.

      Hedelius, J. K., Liu, J., Oda, T., Maksyutov, S., Roehl, C. M., Iraci, L. T., Podolske, J. R., Hillyard, P. W., Liang, J., Gurney, K. R., Wunch, D.,
        and Wennberg, P. O.: Southern California megacity $CO_2$, $CH_4$, and CO flux estimates using ground- and space-based remote sensing and
        a Lagrangian model, Atmospheric Chemistry and Physics, 18, 16 271–16 291, https://doi.org/10.5194/acp-18-16271-2018, https://www.
        atmos-chem-phys.net/18/16271/2018/, 2018.

565   Janssens-Maenhout, G., Crippa, M., Guizzardi, D., Muntean, M., Schaaf, E., Dentener, F., Bergamaschi, P., Pagliari, V., Olivier, J. G. J.,
        Peters, J. A. H. W., van Aardenne, J. A., Monni, S., Doering, U., Petrescu, A. M. R., Solazzo, E., and Oreggioni, G. D.: EDGAR
        v4.3.2 Global Atlas of the three major greenhouse gas emissions for the period 1970–2012, Earth System Science Data, 11, 959–1002,
        https://doi.org/10.5194/essd-11-959-2019, https://essd.copernicus.org/articles/11/959/2019/, 2019.

      Kiel, M., O'Dell, C. W., Fisher, B., Eldering, A., Nassar, R., MacDonald, C. G., and Wennberg, P. O.: How bias correction goes wrong:
570     measurement of XCO2 affected by erroneous surface pressure estimates., Atmospheric Measurement Techniques, 12, 2019.

      Kiel, M., Eldering, A., Roten, D. D., Lin, J. C., Feng, S., Lei, R., Lauvaux, T., Oda, T., Roehl, C. M., Blavier, J.-F., and Iraci, L. T.:
        Urban-focused satellite CO2 observations from the Orbiting Carbon Observatory-3: A first look at the Los Angeles megacity, Remote
        Sensing of Environment, 258, 112 314, https://doi.org/https://doi.org/10.1016/j.rse.2021.112314, https://www.sciencedirect.com/science/
        article/pii/S0034425721000328, 2021.

575   Kort, E. A., Frankenberg, C., Miller, C. E., and Oda, T.: Space-based observations of megacity carbon dioxide, Geophysical Research Letters,
        39, 2012.

      Krings, T., Gerilowski, K., Buchwitz, M., Reuter, M., Tretner, A., Erzinger, J., Heinze, D., Plüger, U., Burrows, J., and Bovensmann, H.:
        MAMAP-a new sperctrometer system for column-averaged methane and carbon dioxide observations from aircraft: retrieval algorithm
        and first inversions for point source emission rates, Atmospheric Measurement Techniques, 4, 1735–1758, 2011.

580   Lama, S., Houweling, S., Boersma, K. F., Eskes, H., Aben, I., Denier van der Gon, H. A., Krol, M. C., Dolman, H., Borsdorff, T., and Lorente,
        A.: Quantifying burning efficiency in megacities using the NO 2/ CO ratio from the Tropospheric Monitoring Instrument (TROPOMI),
        Atmospheric Chemistry and Physics, 20, 10 295–10 310, 2020.

      Landgraf, J., Scheepmaker, R., Borsdorff, T., Hu, H., Houweling, S., Butz, A., Aben, I., Hasekamp, O., et al.: Carbon monoxide total column
        retrievals from TROPOMI shortwave infrared measurements, Atmospheric Measurement Techniques (AMT), 9, 4955–4975, 2016.

585   Laughner, J. L. and Cohen, R. C.: Direct observation of changing NOx lifetime in North American cities, Science, 366, 723–727, 2019.

      Lucchesi, R.: File Specification for GEOS-5 FP-IT (forward processing for instrument teams), Tech. rep., NASA Goddard Space Flight
        Center, Greenbelt, MD, USA,, https://gmao.gsfc.nasa.gov/pubs/docs/Lucchesi865.pdf, last access: 13 October 2020, 2015.

Lutsch, E., Strong, K., Jones, D. B. A., Blumenstock, T., Conway, S., Fisher, J. A., Hannigan, J. W., Hase, F., Kasai, Y., Mahieu, E., Makarova, M., Morino, I., Nagahama, T., Notholt, J., Ortega, I., Palm, M., Poberovskii, A. V., Sussmann, R., and Warneke, T.: Detection and attribution of wildfire pollution in the Arctic and northern midlatitudes using a network of Fourier-transform infrared spectrometers and GEOS-Chem, Atmospheric Chemistry and Physics, 20, 12 813–12 851, https://doi.org/10.5194/acp-20-12813-2020, https://acp.copernicus.org/articles/20/12813/2020/, 2020.

Martin, D. O.: Comment On"The Change of Concentration Standard Deviations with Distance", Journal of the Air Pollution Control Association, 26, 145–147, https://doi.org/10.1080/00022470.1976.10470238, https://doi.org/10.1080/00022470.1976.10470238, 1976.

McKain, K., Wofsy, S. C., Nehrkorn, T., Eluszkiewicz, J., Ehleringer, J. R., and Stephens, B. B.: Assessment of ground-based atmospheric observations for verification of greenhouse gas emissions from an urban region, Proceedings of the National Academy of Sciences, 109, 8423–8428, 2012.

Molod, A., Takacs, L., Suarez, M., and Bacmeister, J.: Development of the GEOS-5 atmospheric general circulation model: evolution from MERRA to MERRA2, Geoscientific Model Development, 8, 1339–1356, https://doi.org/10.5194/gmd-8-1339-2015, https://gmd.copernicus.org/articles/8/1339/2015/, 2015.

Nassar, R., Napier-Linton, L., Gurney, K. R., Andres, R. J., Oda, T., Vogel, F. R., and Deng, F.: Improving the temporal and spatial distribution of CO2 emissions from global fossil fuel emission data sets, Journal of Geophysical Research: Atmospheres, 118, 917–933, 2013.

Nassar, R., Hill, T. G., McLinden, C. A., Wunch, D., Jones, D. B., and Crisp, D.: Quantifying CO2 emissions from individual power plants from space, Geophysical Research Letters, 44, 10–045, 2017.

Nassar, R., Mastrogiacomo, J.-P., Bateman-Hemphill, W., McCracken, C., MacDonald, C. G., Hill, T., O'Dell, C. W., Kiel, M., and Crisp, D.: Advances in quantifying power plant CO2 emissions with OCO-2, Remote Sensing of Environment, 264, 112 579, https://doi.org/https://doi.org/10.1016/j.rse.2021.112579, https://www.sciencedirect.com/science/article/pii/S0034425721002996, 2021.

Oda, T. and Maksyutov, S.: A very high-resolution (1 km×1 km) global fossil fuel $CO_2$ emission inventory derived using a point source database and satellite observations of nighttime lights, Atmospheric Chemistry and Physics, 11, 543–556, https://doi.org/10.5194/acp-11-543-2011, https://www.atmos-chem-phys.net/11/543/2011/, 2011.

Pandis, S. N. and Seinfeld, J. H.: Atmospheric chemistry and physics: From air pollution to climate change, Wiley, 2006.

Pasquill, F.: The estimation of the dispersion of windborne material, Met. Mag., 90, 33, 1961.

Plant, G., Kort, E. A., Murray, L. T., Maasakkers, J. D., and Aben, I.: Evaluating urban methane emissions from space using TROPOMI methane and carbon monoxide observations, Remote Sensing of Environment, 268, 112 756, https://doi.org/https://doi.org/10.1016/j.rse.2021.112756, https://www.sciencedirect.com/science/article/pii/S0034425721004764, 2022.

Reuter, M., Buchwitz, M., Schneising, O., Krautwurst, S., O'Dell, C. W., Richter, A., Bovensmann, H., and Burrows, J. P.: Towards monitoring localized CO 2 emissions from space: co-located regional CO 2 and NO 2 enhancements observed by the OCO-2 and S5P satellites, Atmospheric Chemistry and Physics, 19, 9371–9383, 2019.

Silva, S. J. and Arellano, A.: Characterizing regional-scale combustion using satellite retrievals of CO, NO2 and CO2, Remote Sensing, 9, 744, 2017.

Ummel, K.: CARMA revisited: an updated database of carbon dioxide emissions from power plants worldwide, Center for Global Development Working Paper, 2012.

van Geffen, J., Boersma, K. F., Eskes, H., Sneep, M., ter Linden, M., Zara, M., and Veefkind, J. P.: S5P TROPOMI $NO_2$ slant column retrieval: method, stability, uncertainties and comparisons with OMI, Atmospheric Measurement Techniques, 13, 1315–1335, https://doi.org/10.5194/amt-13-1315-2020, https://www.atmos-meas-tech.net/13/1315/2020/, 2020.

Veefkind, J., Aben, I., McMullan, K., Förster, H., De Vries, J., Otter, G., Claas, J., Eskes, H., De Haan, J., Kleipool, Q., et al.: TROPOMI on the ESA Sentinel-5 Precursor: A GMES mission for global observations of the atmospheric composition for climate, air quality and ozone layer applications, Remote Sensing of Environment, 120, 70–83, 2012.

Wu, D., Lin, J. C., Fasoli, B., Oda, T., Ye, X., Lauvaux, T., Yang, E. G., and Kort, E. A.: A Lagrangian approach towards extracting signals
630    of urban CO 2 emissions from satellite observations of atmospheric column CO 2 (XCO 2): X-Stochastic Time-Inverted Lagrangian Transport model ("X-STILT v1"), Geoscientific Model Development, 11, 4843, 2018.

Wunch, D., Wennberg, P., Toon, G., Keppel-Aleks, G., and Yavin, Y.: Emissions of greenhouse gases from a North American megacity, Geophysical Research Letters, 36, 2009.

Wunch, D., Toon, G. C., Hedelius, J. K., Vizenor, N., Roehl, C. M., Saad, K. M., Blavier, J.-F. L., Blake, D. R., and Wennberg, P. O.:
635    Quantifying the loss of processed natural gas within California's South Coast Air Basin using long-term measurements of ethane and methane, Atmospheric Chemistry and Physics, 16, 14 091–14 105, 2016.

Wunch, D., Wennberg, P. O., Osterman, G., Fisher, B., Naylor, B., Roehl, C. M., O'Dell, C., Mandrake, L., Viatte, C., Kiel, M., Griffith, D. W. T., Deutscher, N. M., Velazco, V. A., Notholt, J., Warneke, T., Petri, C., De Maziere, M., Sha, M. K., Sussmann, R., Rettinger, M., Pollard, D., Robinson, J., Morino, I., Uchino, O., Hase, F., Blumenstock, T., Feist, D. G., Arnold, S. G., Strong, K., Mendonca,
640    J., Kivi, R., Heikkinen, P., Iraci, L., Podolske, J., Hillyard, P. W., Kawakami, S., Dubey, M. K., Parker, H. A., Sepulveda, E., García, O. E., Te, Y., Jeseck, P., Gunson, M. R., Crisp, D., and Eldering, A.: Comparisons of the Orbiting Carbon Observatory-2 (OCO-2) $X_{CO_2}$ measurements with TCCON, Atmospheric Measurement Techniques, 10, 2209–2238, https://doi.org/10.5194/amt-10-2209-2017, https://www.atmos-meas-tech.net/10/2209/2017/, 2017.

York, D., Evensen, N. M., Martınez, M. L., and De Basabe Delgado, J.: Unified equations for the slope, intercept, and standard errors of the
645    best straight line, American Journal of Physics, 72, 367–375, 2004.

Zhao, X., Griffin, D., Fioletov, V., McLinden, C., Cede, A., Tiefengraber, M., Müller, M., Bognar, K., Strong, K., Boersma, F., Eskes, H., Davies, J., Ogyu, A., and Lee, S. C.: Assessment of the quality of TROPOMI high-spatial-resolution $NO_2$ data products in the Greater Toronto Area, Atmospheric Measurement Techniques, 13, 2131–2159, https://doi.org/10.5194/amt-13-2131-2020, https://amt.copernicus.org/articles/13/2131/2020/, 2020.

**Table 1.** Summary of inventory-based emissions estimates for all the cities that were considered. Gridded emissions are summed across the extent of the GHS polygon for each city. For the ODIAC and MACCity inventories, which are provided at a monthly temporal resolution, the estimate is the mean across all 12 months.

| City | 2015 Population [$10^6$] | ODIAC $CO_2$ [Tg/yr] | FFDAS $CO_2$ [Tg/yr] | EDGAR $CO_2$ [Tg/yr] | EDGAR CO [Gg/yr] | MACCity CO [Gg/yr] | EDGAR $NO_2$ [Gg/yr] | MACCity $NO_2$ [Gg/yr] |
|---|---|---|---|---|---|---|---|---|
| Ahmadabad | 6.7 | 15.3 | 12.5 | 6.2 | 68.0 | 58.6 | 15.3 | 4.3 |
| Alexandria | 5.5 | 8.9 | 4.9 | 19.6 | 29.2 | 27.7 | 36.2 | 3.9 |
| Baghdad | 5.4 | 10.7 | 10.0 | 17.4 | 292.5 | 130.0 | 65.4 | 18.9 |
| Buenos Aires | 13.9 | 45.8 | 28.8 | 29.9 | 316.5 | 76.7 | 80.8 | 23.7 |
| Cairo | 19.7 | 38.9 | 39.7 | 37.9 | 122.3 | 274.1 | 66.0 | 35.4 |
| Chicago | 6.8 | 80.8 | 80.0 | 51.1 | 217.2 | 73.8 | 78.4 | 23.9 |
| Dallas | 5.2 | 42.9 | 49.2 | 30.8 | 171.2 | 41.7 | 52.7 | 11.9 |
| Delhi | 26.7 | 97.0 | 68.1 | 41.2 | 549.4 | 889.1 | 100.9 | 53.8 |
| Guangzhou | 40.6 | 302.9 | 300.6 | 177.1 | 1371.0 | 1542.1 | 295.5 | 166.8 |
| Houston | 4.9 | 57.0 | 54.6 | 43.3 | 161.3 | 37.7 | 70.4 | 14.3 |
| Indianapolis | 1.1 | 15.2 | 14.5 | 7.8 | 40.7 | 11.3 | 13.4 | 3.9 |
| Johannesburg | 6.5 | 43.7 | 19.6 | 22.5 | 404.6 | 339.1 | 66.4 | 22.4 |
| Lahore | 10.1 | 9.7 | 6.0 | 6.3 | 252.9 | 128.3 | 28.0 | 6.7 |
| Las Vegas | 2.0 | 20.6 | 16.7 | 10.0 | 42.3 | 6.6 | 19.0 | 3.3 |
| London | 9.6 | 17.4 | 23.1 | 31.2 | 49.7 | 16.9 | 42.0 | 14.7 |
| Los Angeles | 14.3 | 80.8 | 84.1 | 89.9 | 301.4 | 104.7 | 132.0 | 43.3 |
| Madrid | 4.9 | 9.1 | 11.0 | 9.5 | 27.9 | 5.5 | 16.2 | 4.2 |
| Mexico City | 19.6 | 40.0 | 38.4 | 26.1 | 362.8 | 129.9 | 63.5 | 21.8 |
| Moscow | 14.1 | 79.9 | 46.9 | 110.4 | 212.7 | 263.7 | 160.1 | 170.8 |
| Paris | 9.7 | 22.4 | 26.4 | 25.2 | 50.5 | 58.3 | 29.5 | 19.5 |
| Phoenix | 3.6 | 27.1 | 26.9 | 23.1 | 100.9 | 15.0 | 38.3 | 6.7 |
| Riyadh | 5.7 | 101.7 | 92.8 | 68.5 | 136.4 | 22.8 | 131.0 | 13.0 |
| San Francisco | 4.6 | 13.8 | 16.4 | 22.7 | 85.9 | 38.6 | 35.6 | 17.3 |
| Seoul | 21.6 | 122.4 | 99.8 | 96.6 | 286.6 | 380.5 | 141.7 | 47.0 |
| Tehran | 12.5 | 46.8 | 49.1 | 57.7 | 654.2 | 294.4 | 106.1 | 50.8 |
| Toronto | 6.0 | 27.4 | 41.2 | 53.1 | 136.8 | 68.7 | 63.0 | 20.0 |
| Vienna | 1.9 | 6.1 | 6.2 | 8.1 | 12.3 | 2.6 | 10.2 | 1.5 |

**Table 2.** Summary of all the enhancement ratios that were derived using OCO-2/3 and TROPOMI. Instances where a poor linear relation was observed when regressing one set of anomalies onto another are marked by a dash. The number of OCO-2/3 overpasses used to derive $CO:CO_2$ ratios is given first, and the number used to derive $NO_2:CO_2$ ratios is shown in brackets.

| City | No. of OCO-2/3 Overpasses | $CO:CO_2$ Enhancement Ratio [ppb:ppm] | $NO_2:CO_2$ Enhancement Ratio [ppb:ppm] | $NO_2:CO$ Enhancement Ratio [ppb:ppb] |
|---|---|---|---|---|
| Ahmadabad | 3(-) | $12.8 \pm 1.1$ | - | - |
| Alexandria | -(5) | - | $0.40 \pm 0.04$ | $0.018 \pm 0.002$ |
| Baghdad | 4(8) | $6.3 \pm 0.3$ | $0.91 \pm 0.04$ | $0.180 \pm 0.013$ |
| Buenos Aires | 10(10) | $7.9 \pm 0.3$ | $0.57 \pm 0.02$ | $0.048 \pm 0.004$ |
| Cairo | 14(14) | $13.9 \pm 0.9$ | $0.50 \pm 0.02$ | $0.038 \pm 0.001$ |
| Chicago | 5(5) | $13.3 \pm 0.7$ | $0.63 \pm 0.02$ | $0.028 \pm 0.003$ |
| Dallas | 4(4) | $3.7 \pm 0.2$ | $0.18 \pm 0.01$ | $0.032 \pm 0.002$ |
| Delhi | 4(5) | $13.1 \pm 0.5$ | $0.88 \pm 0.04$ | $0.017 \pm 0.001$ |
| Guangzhou | 3(-) | $13.0 \pm 1.6$ | - | $0.016 \pm 0.002$ |
| Houston | -(6) | - | $0.37 \pm 0.02$ | $0.015 \pm 0.001$ |
| Indianapolis | 7(7) | $13.4 \pm 0.9$ | $0.42 \pm 0.03$ | $0.018 \pm 0.003$ |
| Johannesburg | 11(11) | $15.4 \pm 0.5$ | $2.50 \pm 0.15$ | $0.166 \pm 0.012$ |
| Lahore | -(-) | - | - | $0.022 \pm 0.002$ |
| Las Vegas | 11(11) | $8.1 \pm 0.4$ | $0.41 \pm 0.02$ | $0.021 \pm 0.001$ |
| London | 2(2) | $5.8 \pm 0.3$ | $0.53 \pm 0.01$ | $0.075 \pm 0.007$ |
| Los Angeles | 9(9) | $8.3 \pm 0.3$ | $0.32 \pm 0.01$ | $0.030 \pm 0.001$ |
| Madrid | -(10) | - | $0.95 \pm 0.04$ | $0.099 \pm 0.008$ |
| Mexico City | 12(12) | $19.0 \pm 0.8$ | $1.29 \pm 0.05$ | $0.041 \pm 0.003$ |
| Moscow | 5(5) | $12.5 \pm 0.7$ | $1.38 \pm 0.07$ | $0.083 \pm 0.007$ |
| Paris | 6(6) | $12.6 \pm 1.1$ | $0.70 \pm 0.04$ | $0.054 \pm 0.006$ |
| Phoenix | 20(20) | $6.6 \pm 0.2$ | $0.30 \pm 0.01$ | $0.028 \pm 0.001$ |
| Riyadh | 8(-) | $11.2 \pm 0.5$ | - | $0.372 \pm 0.029$ |
| San Francisco | -(7) | - | $0.26 \pm 0.02$ | $0.009 \pm 0.001$ |
| Seoul | -(4) | - | $0.71 \pm 0.04$ | $0.069 \pm 0.008$ |
| Tehran | 13(13) | $23.9 \pm 1.3$ | $1.94 \pm 0.18$ | $0.052 \pm 0.001$ |
| Toronto | 1(1) | $10.7 \pm 1.1$ | $0.80 \pm 0.07$ | $0.026 \pm 0.004$ |
| Vienna | 2(-) | $7.2 \pm 0.6$ | - | - |

**Table 3.** Summary of all the $NO_2:CO_2$ and $NO_2:CO$ enhancement ratios that were derived using OCO-2/3 and TROPOMI, with the correction for $NO_2$ lifetime added.

| City | No. of OCO-2/3 Overpasses | $NO_2:CO_2$ Enhancement Ratio [ppb:ppm] | $NO_2:CO$ Enhancement Ratio [ppb:ppb] |
|---|---|---|---|
| Alexandria | 5 | $0.45 \pm 0.10$ | $0.019 \pm 0.005$ |
| Baghdad | 8 | $1.14 \pm 0.23$ | $0.214 \pm 0.045$ |
| Buenos Aires | 10 | $1.26 \pm 0.25$ | $0.074 \pm 0.015$ |
| Cairo | 14 | $0.86 \pm 0.17$ | $0.093 \pm 0.019$ |
| Chicago | 5 | $1.24 \pm 0.25$ | $0.047 \pm 0.010$ |
| Dallas | 4 | $0.32 \pm 0.06$ | $0.123 \pm 0.025$ |
| Delhi | 5 | $6.48 \pm 1.30$ | $0.045 \pm 0.009$ |
| Guangzhou | 3 | - | $0.516 \pm 0.103$ |
| Houston | 6 | $0.77 \pm 0.15$ | $0.061 \pm 0.012$ |
| Indianapolis | 7 | $0.57 \pm 0.12$ | $0.032 \pm 0.007$ |
| Johannesburg | 11 | $2.74 \pm 0.57$ | $0.179 \pm 0.038$ |
| Lahore | 11 | - | $0.074 \pm 0.015$ |
| Las Vegas | 11 | $0.90 \pm 0.18$ | $0.054 \pm 0.011$ |
| London | 2 | $0.67 \pm 0.13$ | $0.121 \pm 0.025$ |
| Los Angeles | 9 | $0.69 \pm 0.14$ | $0.057 \pm 0.011$ |
| Madrid | 10 | $1.78 \pm 0.36$ | $0.213 \pm 0.043$ |
| Mexico City | 12 | $3.95 \pm 0.79$ | $0.146 \pm 0.029$ |
| Moscow | 5 | $2.52 \pm 0.51$ | $0.166 \pm 0.034$ |
| Paris | 6 | $1.30 \pm 0.26$ | $0.204 \pm 0.041$ |
| Phoenix | 20 | $2.06 \pm 0.41$ | $0.375 \pm 0.075$ |
| Riyadh | 8 | - | $0.522 \pm 0.108$ |
| San Francisco | 7 | $0.32 \pm 0.07$ | $0.010 \pm 0.002$ |
| Seoul | 4 | $1.46 \pm 0.30$ | $0.323 \pm 0.065$ |
| Tehran | 13 | $4.26 \pm 0.87$ | $0.080 \pm 0.016$ |
| Toronto | 1 | $2.46 \pm 0.50$ | $0.055 \pm 0.012$ |